chemosensors

MDPI

Article

Enhanced NO_2-Sensing Properties of Au-Loaded Porous In_2O_3 Gas Sensors at Low Operating Temperatures

Taro Ueda [1,*], Inci Boehme [2], Takeo Hyodo [1], Yasuhiro Shimizu [1], Udo Weimar [2] and Nicolae Barsan [2]

[1] Graduate School of Engineering, Nagasaki University, 1-14 Bunkyo-machi, Nagasaki 852-8521, Japan; hyodo@nagasaki-u.ac.jp (T.H.); shimizu@nagasaki-u.ac.jp (Y.S.)

[2] Institute of Physical and Theoretical Chemistry, Eberhard Karls University of Tuebingen, D-72076 Tübingen, Germany; inci.boehme@ipc.uni-tuebingen.de (I.B.); upw@ipc.uni-tuebingen.de (U.W.); nb@ipc.uni-tuebingen.de (N.B.)

* Correspondence: taroueda@nagasaki-u.ac.jp

Received: 11 June 2020; Accepted: 19 August 2020; Published: 20 August 2020

Abstract: NO_2-sensing properties of semiconductor gas sensors using porous In_2O_3 powders loaded with and without 0.5 wt% Au (Au/In_2O_3 and In_2O_3 sensors, respectively) were examined in wet air (70% relative humidity at 25 °C). In addition, the effects of Au loading on the increased NO_2 response were discussed on the basis of NO_2 adsorption/desorption properties on the oxide surface. The NO_2 response of the Au/In_2O_3 sensor monotonically increased with a decrease in the operating temperature, and the Au/In_2O_3 sensor showed higher NO_2 responses than those of the In_2O_3 sensor at a temperature of 100 °C or lower. In addition, the response time of the Au/In_2O_3 sensor was much shorter than that of the In_2O_3 sensor at 30 °C. The analysis based on the Freundlich adsorption mechanism suggested that the Au loading increased the adsorption strength of NO_2 on the In_2O_3 surface. Moreover, the Au loading was also quite effective in decreasing the baseline resistance of the In_2O_3 sensor in wet air (i.e., increasing the number of free electrons in the In_2O_3), which resulted in an increase in the number of negatively charged NO_2 species on the In_2O_3 surface. The Au/In_2O_3 sensor showed high response to the low concentration of NO_2 (ratio of resistance in target gas to that in air: ca. 133 to 0.1 ppm) and excellent NO_2 selectivity against CO and ethanol, especially at 100 °C.

Keywords: semiconductor gas sensor; NO_2; porous In_2O_3; loading of Au; ultrasonic spray pyrolysis; Freundlich adsorption isotherm

1. Introduction

Semiconductor gas sensors were firstly commercialized as gas leak detectors in the 1960s [1], and additional studies have been carried out in order to detect various gases such as alcohol and volatile organic compounds (VOCs) [2–4]. The inhalation of even low concentration of NO_2 causes serious damage to the respiratory system [5–7]. Therefore, the United States Environmental Protection Agency (EPA) sets the regulatory value of 0.053 ppm NO_2 as an air quality standard [8]. The NOx concentration in atmospheric environment has been measured by means of large and expensive analytical instruments based on a chemiluminescence method [9,10]. Therefore, the development of highly sensitive semiconductor NO_2 sensors has been expected all over the world. Among the various semiconducting metal oxides, SnO_2 [11–13], WO_3 [5,14,15], In_2O_3 [16–26], and ZnO [27–29] are well known as semiconducting NO_2-sensing materials. In addition, the structural modification of the sensing layer is one of important techniques in order to enhance the sensing properties. For example, Kim et al. fabricated nanowired SnO_2 on an alumina substrate by a chemical vapor deposition

(CVD) method, and it showed 10 times higher NO_2 response than powdered SnO_2 synthesized by a conventional precipitation method. The detection limit of NO_2 was as low as 50 ppb [12]. Yang et al. investigated the relationship between crystallite size of WO_3 particles and their NO_2 response, and they clarified that the WO_3 particles with a diameter of 7–9 nm detected even 40 ppb NO_2 [14]. Xu et al. successfully synthesized flower-like structured In_2O_3 by a hydrothermal method, and clarified the fabricated sensor also detected 40 ppb NO_2 [19]. Dilonardo et al. reported that rod-like ZnO were synthesized by controlling the annealing temperature of the precursor gel obtained by a precipitation method, and the fabricated sensor detected 200 ppb NO_2 [29]. The operation of semiconductor gas sensors is based on the change in electrical resistance of the sensing materials by the gas exposure. When the sensors are in air, oxygen adsorbs on the oxide surface and traps a certain number of free electrons in the conduction band of the oxide. When the sensor is exposed to reducing gases (e.g., CO or hydrocarbons), the oxygen adsorbates react with these gases to desorb from the oxide surface. Simultaneously, the free electrons go back to the oxide, which results in a decrease in the sensor resistance. On the other hand, when the sensor is exposed to the oxidizing gases (e.g., NO_2, O_3, and Cl_2), a certain number of free electrons is captured by their negatively charged adsorption [30]. This results in an increase in the sensor resistance. Among some attractive NO_2-sensing materials, In_2O_3 has the advantage of the detection towards oxidizing gases at low temperatures [16,31,32] due to its high conductivity [17,18,23,32,33].

We previously reported that porous In_2O_3 powders could be fabricated by ultrasonic spray pyrolysis using a precursor solution containing $In(NO_3)_3$ and polymethylmethacrylate (PMMA) microspheres (Soken Chem. & Eng. Co., Ltd. (Tokyo, Japan), typical particle size (ps): ca. 150 nm in diameter) as a template, and that the sensors fabricated by employing these In_2O_3 powders showed much higher NO_2 responses and quicker NO_2 response/recovery speeds than a conventional In_2O_3 sensor prepared by the similar technique employing a PMMA-free $In(NO_3)_3$ aqueous solution [34,35]. In addition, we successfully synthesized smaller PMMA microspheres (ps: ca. 26 or ca. 70 nm) by ultrasonic-assisted emulsion polymerization technique using an appropriate amount of methyl methacrylate monomer and sodium lauryl sulfate (SLS) as a surfactant. The fabricated sensors using the In_2O_3 powders fabricated by ultrasonic spray pyrolysis employing the smaller PMMA microspheres as a template in a precursor solution largely enhanced the NO_2 response [36,37]. Table 1 summarizes typical examples of NO_2 detection using In_2O_3-based gas sensors [17–26,38]. In addition to the structural modifications of the sensing layer such as flower-like, porous nanosheet, and nanowire structure [17–19], the loading of noble metal such as Au, Pd, and Pt onto the oxides is another important technique to realize a high sensor response [20–26]. The effects are known as chemical and/or electronic sensitization phenomena [39]. Li et al. reported that the loading of 0.5 wt% Au on the porous In_2O_3 fabricated by a casting method using the mesoporous silica as a template increased the NO_2 response of the pristine porous In_2O_3 by 7.1 times [20]. Wang et al. synthesized a macroporous In_2O_3 powders which contains periodic voids with an average diameter of 210 nm by employing PMMA microspheres as a template, and they clarified that the 0.5 wt% Pd loading on the macroporous In_2O_3 drastically enhanced the NO_2 response [24]. We also reported that the Au loading on the porous In_2O_3 fabricated by ultrasonic spray pyrolysis using a precursor solution containing $In(NO_3)_3$ and PMMA microspheres was quite effective in increasing the NO_2 response at operating temperatures of 200 °C or lower in dry air, while the loading of Pd or Pt did not show any positive effects. In addition, our results suggested that Au loading promoted the adsorption of the negatively charged NO_2 species on the bottom part of the sensing layer, leading to an increase in the NO_2 response. The 0.5 wt% Au-loaded In_2O_3 sensor showed the highest response to 0.25 ppm NO_2 at 30 °C among all the sensors in Table 1 [38]. However, their sensing properties to NO_2 are not yet confirmed under humidified atmosphere, especially at lower temperatures. In addition, the Au loading seems to have a great influence on the number and state of NO_2 adsorbates on the oxide surface [38]. In this study, the NO_2-sensing properties of the Au-loaded and -unloaded porous In_2O_3 sensors have been measured in wet air, and the effects of the Au loading on the sensing properties also have been discussed on the basis of NO_2 adsorption properties on the oxide surface.

Table 1. Typical examples of NO_2 detection using In_2O_3-based gas sensors.

Material of Sensing Layer	Fabrication Technique	Structure of In_2O_3	Appropriate Operating Temperature/°C	NO_2 Response [a]	NO_2 Detection Limit/ppm	Year	Ref.
In_2O_3	Hydrothermal synthesis	Flower-like particle	150	74 (0.5 ppm)	0.04	2013	[17]
In_2O_3	Hydrothermal synthesis	Porous nanosheet	250	164 (50 ppm)	1	2015	[18]
In_2O_3	Hydrothermal synthesis	Nanofiber	250	2.57 (1 ppm)	1	2008	[19]
Au/In_2O_3	Casting using SBA-15 [b]	Porous particle	65	472 (0.5 ppm)	0.01	2018	[20]
Au/In_2O_3	Magnetron sputtering	Thin film	350	142 (10 ppm)	10	2001	[21]
Au/In_2O_3	Hydrothermal synthesis	Core–shell	300	15 (100 ppm)	100	2016	[22]
Pt/In_2O_3	Electrospinning	Nanowire	80	19.2 (0.5 ppm)	0.01	2018	[23]
Pd/In_2O_3	Casting using PMMA [c]	Porous particle	Room temperature	980 (0.5 ppm)	0.1	2018	[24]
Zn/In_2O_3	Electrospinning	Nanowire	50	130 (5 ppm)	0.05	2020	[25]
Zr/In_2O_3	Casting using SBA-15 [b]	Porous particle	75	169 (1 ppm)	0.02	2017	[26]
Au/In_2O_3	Ultrasonic spray pyrolysis	Porous particle	30	10000 (0.25 ppm)	0.025	2019	[38]

[a] NO_2 response: the ratio (R_g/R_a) of resistance in the target gas (R_g) to that in air (R_a). [b] SBA-15: name of mesoporous silica. [c] PMMA: polymethylmethacrylate.

2. Materials and Methods

2.1. Preparation of In_2O_3 Powders by Ultrasonic Spray Pyrolysis

PMMA microspheres (ps: ca. 70 nm), which were synthesized by ultrasonic-assisted emulsion polymerization [38], were used as a polymer template. The aqueous dispersion containing the PMMA microspheres (37.5 cm^3) and $In(NO_3)\cdot 3H_2O$ (1.77 g) was mixed with pure water (62.5 cm^3), and the mixture was served as an aqueous precursor solution. In order to load 0.5 wt% Au nanoparticles on the In_2O_3 powder, $HAuCl_4\cdot 4H_2O$ (3.5 mg) was added to the precursor solution. Figure 1 shows a schematic drawing of an apparatus of ultrasonic spray pyrolysis. Precursor mists were obtained by ultrasonication of the aqueous precursor solution in a plastic container equipped with a polyethylene thin film at one end, which was perpendicularly set over an ultrasonic vibrator (Honda Electric Co., Ltd., Tokyo Japan, HM-303N, 2.4 MHz) at a distance of 0.5–1.0 cm in water. A specially designed mist supplier for the ultrasonic spray pyrolysis was used to obtain uniform mists of the precursor solution. Only small droplets separated in a glass vessel were fed into an electric furnace heated at 1000 °C under flowing air (1500 cm^3 min^{-1}). The diameter of the droplets supplied by ultrasonic vibrator was analyzed by a phase doppler interferometer (PDI, Seika Co., Ltd., Tokyo, Japan, PDI-100MD). As the mists were instantly heated at the electric furnace, the evaporation of water and the thermal decomposition of $In(NO_3)_3$ and PMMA microspheres simultaneously occurred, and spherical In_2O_3 powders were produced in the electric furnace under the air flow. The thermal decomposition of $HAuCl_4$ also occurred at the same time with those of the $In(NO_3)_3$ and PMMA microspheres, and Au was dispersed in the In_2O_3 powders. The detail of the ultrasonic spray pyrolysis was already reported in our previous paper [38]. The obtained porous powders loaded with and without Au were denoted as Au/In_2O_3 and In_2O_3, respectively.

2.2. Fabrication of Thick Film Sensors and Measurement of Their Gas Sensing Properties

The prepared In_2O_3 or Au/In_2O_3 powder was ground with 1,2-propanediol (Sigma-Aldrich (St. Louis, MO, USA)) by using an agate mortar, and the obtained paste was screen-printed on an Al_2O_3 substrate equipped with a pair of interdigitated Pt electrodes (gap size: ca. 500 μm). After being dried overnight at 80 °C, it was calcined at 500 °C for 10 min in ambient air. The obtained sensor was denoted as an In_2O_3 or Au/In_2O_3 sensor. Figure S1 shows a schematic drawing of (a) sensor element and (b) gas-sensing measurement system. The sensor was mounted in a polytetrafluoroethylene (PTFE) chamber and test gases were supplied using a computer-operated gas-mixing system (the total flow rate was constantly held at 200 cm^3 min^{-1}). The sensing properties of these sensors were measured to NO_2 (0.1–5 ppm) balanced with wet air (70% relative humidity (RH) at 25 °C) at operating temperatures between 30 and 300 °C, which were controlled by using a Pt heater on the back side of the sensor substrate. The magnitude of response to NO_2 was defined as the ratio (R_g/R_a) of resistance in the target gas (R_g) to that in air (R_a), while the magnitude of response to ethanol or CO was defined as R_a/R_g.

The 70% response and recovery times (t_{70res} and t_{70rec}) were defined as the time necessary to reach 70% of the steady state value of R_g and R_a, respectively. In order to discuss NO_2 selectivity against other gases, the magnitude of responses (R_g/R_a or R_a/R_g) were divided by their gas concentrations, and the calculated values (normalized responses) were compared.

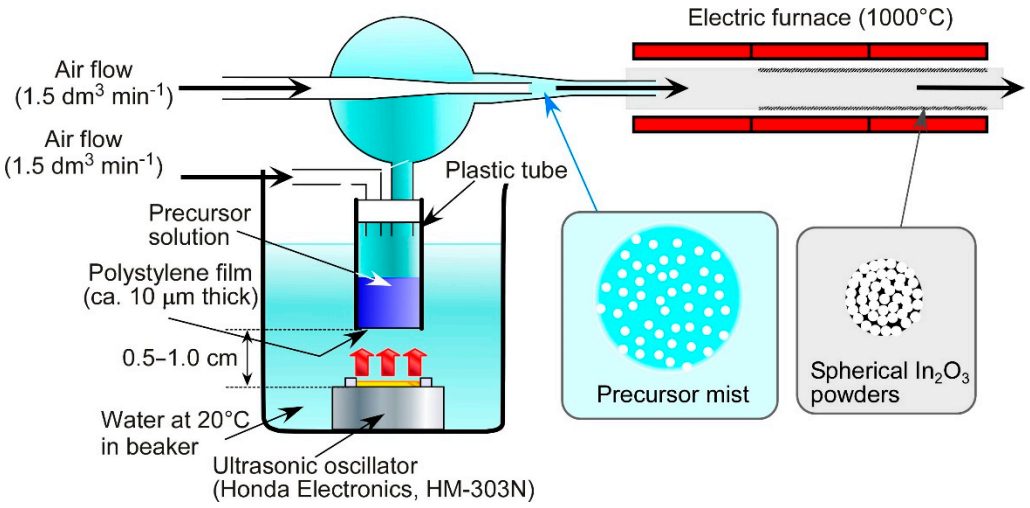

Figure 1. Schematic drawing of an apparatus of ultrasonic spray pyrolysis.

3. Results and Discussion

Figure S2 shows particle size distribution of the precursor mists containing PMMA microspheres and In $(NO_3)_3$, which were prepared by the ultrasonic vibrator. Most of the precursor mists were less than 10 μm in diameter, and the mean diameter was ca. 5 μm. On the other hand, the instantaneous heat treatment of the mists under flowing air in the electric furnace at 1000 °C produced submicron-sized In_2O_3 powders, and the diameter was 10% or less of the mists, as shown in the SEM photographs (Figure 2a). In addition, a well-developed porous structure was observed on the surface of both the In_2O_3 and Au/In_2O_3 powders, because the thermal decomposition of the PMMA microspheres and In $(NO_3)_3$ simultaneously occurred along with the evaporation of water, and only In_2O_3 remained as a solid. The exact same In_2O_3 and Au/In_2O_3 powders were used in our previous study [38] and, thus, the following discussion was developed by utilizing the already analyzed findings. The pore diameter calculated from N_2 adsorption isotherm of the In_2O_3 powder was around 80 nm, which reflected the diameter of the PMMA microspheres as a template (ca. 70 nm) [38]. On the other hand, the Au loading on the In_2O_3 powder had little effect on the particle size and the well-developed porous structure, as shown in Figure 2b. Their specific surface area of the In_2O_3 and Au/In_2O_3 powders confirmed by the Brunauer–Emmett–Teller (BET) method using N_2-adsorption isotherm were 26.3 m^2/g and 23.7 m^2/g, respectively, which was much larger than that of the conventional In_2O_3 powder prepared by the same preparation technique employing a PMMA-free $In(NO_3)_3$ aqueous solution (4.0 m^2/g) [38]. It was already confirmed that the crystal structure of the In_2O_3 and Au/In_2O_3 powders was cubic by X-ray diffraction analysis and that no Au phase was in the XRD spectrum of the Au/In_2O_3 powder [38]. The chemical state of the surface of Au/In_2O_3 powders was also already characterized by X-ray photoelectron spectroscopy (XPS), and two peaks corresponding to $Au4f_{7/2}$ (ca. 83.9 eV) and $Au4f_{5/2}$ (ca. 87.6 eV) showed the chemical state of Au loaded on the In_2O_3 was metal [38]. In addition, transmission electron microscopy (TEM) photographs also showed that the Au nanoparticle with a diameter of less than 10 nm was highly dispersed on the Au/In_2O_3 powders, while a quite large Au agglomerate with a diameter of ca. 22 nm was also observed when the loading amount of Au was increased to 5 wt% [38]. Therefore, these results concluded that a certain amount of Au could be loaded on the In_2O_3 surface.

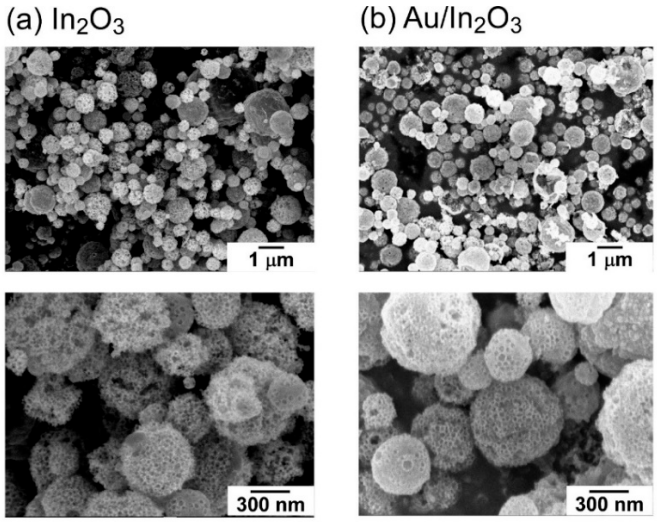

Figure 2. SEM photographs of (**a**) In_2O_3 and (**b**) Au/In_2O_3 powders.

Figure 3 shows the response transients of the In_2O_3 and Au/In_2O_3 sensors to NO_2 (0.6–5 ppm) in wet air at operating temperatures between 30 and 300 °C. The baseline resistance in wet air was decreased by the Au loading at all examined temperatures, although the value was not completely stabilized during this period probably due to slow adsorption behavior of oxygen and water vapor. The resistance of the two sensors was increased abruptly by the injection of 0.6 ppm NO_2 into wet air, and their resistance values steadily increased with an increase in the NO_2 concentration. In addition, the response time of the two sensors tended to decrease with a rise in the operating temperature. The Au/In_2O_3 sensor showed a fast response speed especially at 30 °C when compared to that of the In_2O_3 sensor. However, the baseline resistance did not recover to the initial value probably due to slow NO_2 desorption, especially at a low temperature of 200 °C or lower. On the other hand, the magnitude of NO_2 responses of both the sensors were relatively higher than those of the variation in baseline resistance and, thus, we further discussed the effects of Au loading on the NO_2 sensing properties of these sensors.

Figure 4 shows temperature dependences of the magnitude of response to 0.6 and 5 ppm NO_2 and response time (t_{70res}) to 0.6 ppm NO_2 of the In_2O_3 and Au/In_2O_3 sensors in wet air. The NO_2 response of the In_2O_3 sensor increased with a rise in the operating temperature from 30 to 100 °C, while it decreased with a rise in the temperature above 100 °C. Thus, the highest NO_2 response was observed at 100 °C. On the other hand, the Au/In_2O_3 sensor showed the highest response to NO_2 at 30 °C, and the NO_2 response monotonically decreased with a rise in the operating temperature. As a consequence, the Au/In_2O_3 sensor showed higher NO_2 responses than those of the In_2O_3 sensor at a temperature of 100 °C or lower. Our previous study also showed that the NO_2 responses of In_2O_3 and Au/In_2O_3 sensors respectively decreased and increased with a decrease in the operating temperature lower than 200 °C in dry air [38]. Therefore, the Au loading was effective in increasing the NO_2 response at low operating temperatures, in spite of the presence or absence of humidity. Several researchers also reported an increase in the NO_2 response of the semiconductor gas sensors by Au loading onto metal oxides, and they suggested an increase in the adsorption amount of the negatively charged NO_2 species as a result of spillover effects [40–42]. Therefore, relationships between the adsorption number of the negatively charged NO_2 species on the sensing layer and the sensing properties induced by the Au loading were discussed later.

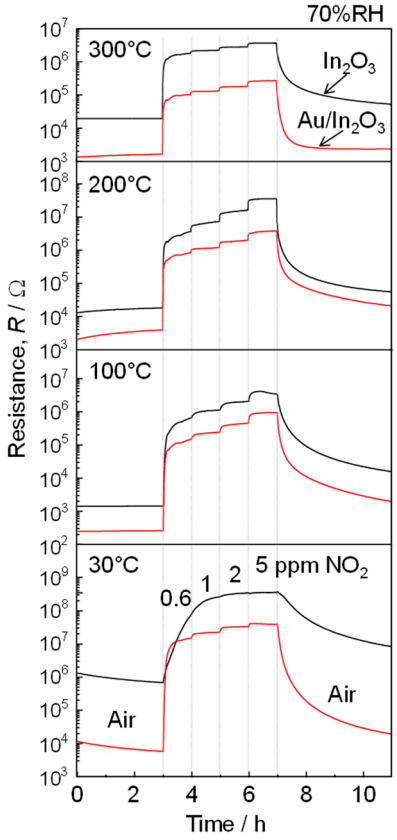

Figure 3. Response transients of the In_2O_3 and Au/In_2O_3 sensors to NO_2 (0.6, 1, 2, 5 ppm) in wet air (70%RH at 25 °C) at 30, 100, 200, and 300 °C.

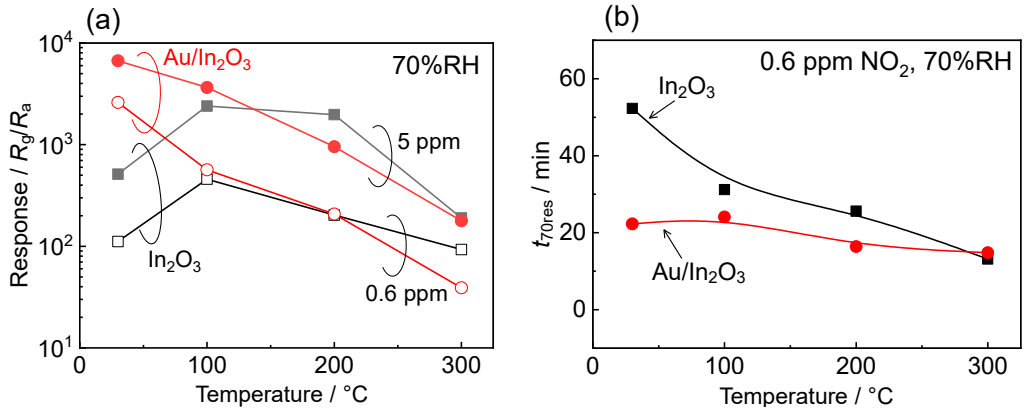

Figure 4. (**a**) Variations in response of the In_2O_3 and Au/In_2O_3 sensors to 0.6 and 5 ppm NO_2 and (**b**) variations in 70% response time (t_{70res}) of the In_2O_3 and Au/In_2O_3 sensors to 0.6 ppm NO_2 in wet air (70%RH at 25 °C) with operating temperature.

On the other hand, it is generally known that a certain amount of NO_2 partially converts to NO toward the thermodynamic equilibrium between them during the gas diffusion, especially at temperatures higher than 200 °C, and the conversion ratio increases with a rise in temperature [43,44]. For example, Miura et al. reported that the NiO-based powders increased the efficiency of the catalytic conversion from NO_2 to NO [43]. Therefore, it was expected that if the loading of Au on the In_2O_3 also accelerated the conversion ratio of NO_2 to NO, then the effective concentration of NO_2 at the bottom part of the sensing layer of the Au/In_2O_3 sensor was considered to become smaller than that of the In_2O_3 sensor at temperatures of 200 °C or larger. Since the sensor response of semiconductor gas sensors

arises from the resistance change at the bottom part of the sensing layer between the interdigitated Pt electrodes, this can be reasonable explanation for lower NO_2 responses of the Au/In_2O_3 sensor at higher operating temperatures (200 and 300 °C). The response time (t_{70res}) value of the In_2O_3 sensor at 30 °C was the largest among all t_{70res} values at every temperature examined. In addition, the t_{70res} value of the Au/In_2O_3 sensor at 30 °C was much smaller than that of the In_2O_3 sensor, even though the magnitude of response of the Au/In_2O_3 sensor at 30 °C was much higher than that of the In_2O_3 sensor. This is probably because the loading of Au accelerated the adsorption of negatively charged NO_2 species on the bottom part of the sensing layer of the Au/In_2O_3 sensor, even at the low operating temperature. On the other hand, the recovery time (t_{70rec}) value of the Au/In_2O_3 sensor at 30 °C was much smaller than that of the In_2O_3 sensor as shown in Figure S3. Therefore, the loading of Au also accelerated desorption of NO_2 at the low operating temperature. In addition, the desorption rate of NO_2 seems to be much slower than the adsorption rate of NO_2 on the Au/In_2O_3 surface.

In order to clarify the magnitude of the NO_2 adsorption of the In_2O_3 and Au/In_2O_3 sensors, the relationship between their steady-state resistances and the NO_2 concentrations were examined. Since the transfer of the free electrons to NO_2 on the oxide surface contributes to the sensor response, the chemical adsorption of NO_2 should be considered for the discussions, as shown in Equation (1) [45].

$$NO_2 + e^- \rightleftarrows NO_2^- \quad (1)$$

The NO_2 response is generally determined by the equilibrium between the adsorption of NO_2 surface (kinetic constant of adsorption; k_a) and the desorption of the negatively charged NO_2 species (kinetic constant of desorption; k_d) on the oxide. Srivastava et al. considered the Freundlich adsorption mechanism as a gas adsorption process on the oxide surface coupled with the Schottky barrier model of the conduction mechanism [46]. Based on the mechanism, the relationship between the sensor resistance and NO_2 concentration was fitted using the following equation:

$$\Delta R = a \times x^b \quad (2)$$

where x is the concentration of NO_2, ΔR is the resistance difference (R_g–R_a) of the sensors, and a and b are indicators of adsorption capacity and strength, respectively [47,48]. The calculated values of a and b are summarized in Table 2 together with the values of the determination coefficient (r) of the regression curve based on Equation (2). Figure 5 shows the NO_2 concentration (x) dependence of ΔR of the In_2O_3 and Au/In_2O_3 sensors at 100 °C in wet air. The successive NO_2 exposure (0.6–5.0 ppm NO_2) to these sensors was repeated twice. The values of r at temperatures above 100 °C were high enough to discuss the correlation between the sensor resistances and the NO_2 concentrations based on Equation (2). On the contrary, the values of r at 30 °C were too low to discuss b value, especially for the In_2O_3 sensor, probably due to slow adsorption properties of NO_2 on the oxide surface.

Table 2. Comparison of a and b values and correlation coefficients (r) of the In_2O_3 and Au/In_2O_3 sensors in wet air (70%RH at 25 °C) at 30, 100, 200, and 300 °C.

		30 °C			100 °C			200 °C			300 °C		
Sensor	**The Order of NO_2 Exposure**	***a***	***b***	***r***	***a***	***b***	***r***	***a***	***b***	***r***	***a***	***b***	***R***
In_2O_3	1st	2.10×10^8	0.38	0.637	1.15×10^6	0.69	0.987	7.65×10^6	0.96	0.996	2.21×10^6	0.33	0.996
	2nd	2.63×10^8	0.38	0.540	1.82×10^6	0.68	0.992	11.2×10^6	0.89	0.996	2.39×10^6	0.29	1.000
Au/In_2O_3	1st	2.23×10^7	0.37	0.890	2.44×10^5	0.84	0.999	1.20×10^6	0.72	1.000	9.97×10^4	0.45	0.993
	2nd	2.71×10^7	0.31	0.889	4.51×10^5	0.78	0.999	1.62×10^6	0.70	0.998	15.7×10^4	0.41	1.000

Since the chemical adsorption of negatively charged NO_2 species mainly contributes to the sensor resistance, consideration of NO_2 chemisorption up to the single-layer formation is sufficient. Therefore, the b value should be not greater than 1. In addition, the large b value shows the strong adsorption of NO_2 on the oxide surface, which means the large increase ratio of the adsorption amount of the

negatively charged NO_2 species. Furthermore, the increase ratio enhanced with an increase in the NO_2 concentration, leading to an increase in the NO_2 response. In fact, the *b* value of the Au/In_2O_3 sensor at 100 °C was larger than that of the In_2O_3 sensor, and the Au/In_2O_3 sensor showed higher NO_2 response than that of the In_2O_3 sensor at 100 °C. In addition, the large difference of the magnitude of response to 5 ppm NO_2 between the Au/In_2O_3 sensor and In_2O_3 sensor at 100 °C in comparison with the one to 0.6 ppm NO_2 can be explained by the larger *b* value (see Figure 4a). These facts explain that the notion that the larger *b* value of the Au/In_2O_3 sensor was an important factor in improving the NO_2 response of the Au/In_2O_3 sensor at 100 °C. In addition, the rise in temperature from 100 to 200 °C increased the *b* value of the In_2O_3 sensor, while it slightly decreased the *b* value of the Au/In_2O_3 sensor. However, the NO_2 responses of both the In_2O_3 and Au/In_2O_3 sensors at 200 °C were lower than those at 100 °C. This is probably due to broadened distribution of various energy levels of NO_2 species by an increase in their thermal motion with a rise in the temperature. Figure S4 shows schematic illustrations of the variations in Gibbs energy diagram for the chemical adsorption of NO_2 over the In_2O_3 and Au/In_2O_3 surfaces with temperature and NO_2 concentration. The number of negatively charged NO_2 species on these surfaces, which reflects the NO_2 response as shown in Figure 4a, is determined by the equilibrium between the adsorption of NO_2 on the oxide surface and the desorption of the negatively charged NO_2 species. The Gibbs energy of the negatively charged NO_2 species is lower than that of gaseous NO_2, and thus the large number of gaseous NO_2 molecules adsorbs on the oxide surface immediately after NO_2 is injected into wet air. In addition, the Gibbs energy of the negatively charged NO_2 species increases with an increase in the NO_2 concentration because of the decrease in the high adsorption affinity sites. Therefore, the difference in the adsorption Gibbs energy (ΔG) decreases with an increase in NO_2 concentration due to the decrease in the facile adsorption sites. On the other hand, the loading of Au catalytically decreases the activation energy (E_a) of the NO_2 adsorption/desorption process. Based on these considerations, a larger increase in the k_d value than the k_a value is expected by the broadened distribution of energy levels of negatively charged NO_2 species with a rise in temperature (compare Figure S4(ai) with Figure S4(aiii); Figure S4(bi) with Figure S4(biii)). Therefore, the adsorption amount of negatively charged NO_2 species on the In_2O_3 surface as well as the Au/In_2O_3 surface seems to decrease with a rise in temperature, leading to a decrease in their NO_2 response, as shown in Figure 4a. In addition, the magnitude of response of the In_2O_3 sensor to 5 ppm NO_2 at 200 °C was comparable to that at 100 °C, while the response to 0.6 ppm NO_2 at 200 °C was much smaller than that at 100 °C (see Figure 4a). This fact explains that the adsorption amount of negatively charged NO_2 species on the In_2O_3 surface largely increased with an increase in the NO_2 concentration at 200 °C in comparison with the case at 100 °C, which corresponded to a higher *b* value at 200 °C (see Table 2). The ΔG decreases from $\Delta G_2'$ to $\Delta G_2''$ and then the k_d value increases with an increase in the NO_2 concentration, which decreases the *b* value. On the other hand, the *b* value increases with an increase in the broadened distribution of energy levels of negatively charged NO_2 species. In this case, the effect of the decrease in the ΔG on the *b* value is overwhelmed by that of the broader distribution of the energy level, and this is the reason why the response of the In_2O_3 sensor to 5 ppm NO_2 at 200 °C was comparable to that at 100 °C (compare Figure S4(ai,aii) with Figure S4(aiii,aiv)). However, the *b* value of the Au/In_2O_3 sensor was decreased by a rise in temperature from 100 to 200 °C (see Table 2). This is probably because the decreased E_a value resulted in a decrease in the energy gap for k_d ($E_a + \Delta G_2''$; compare Figure S4(bi,bii) with Figure S4(biii,biv)) and, thus, the desorption reaction of negatively charged NO_2 species at 200 °C was largely accelerated with increasing NO_2 concentration in comparison with the case at 100 °C. Therefore, the adsorption amount of negatively charged NO_2 species on the Au/In_2O_3 surface largely increased with an increase in the NO_2 concentration at 200 °C in comparison with the case at 100 °C, leading a decrease in the *b* value (see Table 2). However, we also have to consider the adsorption properties of oxygen. The sensor resistance is largely influenced also by the adsorption of negatively charged oxygen together with the adsorption of negatively charged NO_2. Barsan et al. reported that adsorption states of oxygen on the oxide surface at 100 °C and 200 °C are O_2^- and O^-, respectively [49]. In addition, adsorption of water vapor on the oxide surface also

affects the NO_2 sensing properties. For example, Roso et al. reported that the water vapor adsorbed on the oxide surface enhanced the adsorption properties of NO_2, especially at a low operating temperature of 130 °C [50]. In addition, the *b* values in the 2nd NO_2 exposure to both the sensors were smaller than those in 1st NO_2 exposure. Considering that the sensor resistances did not recover to the initial baseline resistance, a certain amount of NO_2 adsorbed was expected to remain on the oxide surface, even when the second NO_2 exposure was started. This indicates that the adsorption strength of NO_2 is higher than that of oxygen on both the oxide surfaces. In addition, the *a* value of the Au/In_2O_3 sensor was smaller than that of the In_2O_3 sensor, but the Au/In_2O_3 sensor showed higher NO_2 responses at lower operating temperatures. Thus, it appears that the calculated *a* values do not exactly show the adsorption capacity of NO_2 on the oxide surface. Namely, we have to consider the decrease in the baseline resistance by the Au loading and positively charged chemisorption of water vapor as a result of the reaction of water with lattice oxygen, while the adsorption species is negative (i.e., OH^-) [49]. In fact, the *a* values were independent of the change in operating temperature, and the *a* values of the second response were larger than those of the first response. Therefore, it is difficult to discuss the differences in the *a* values between the In_2O_3 sensor and the Au/In_2O_3 sensor more in detail.

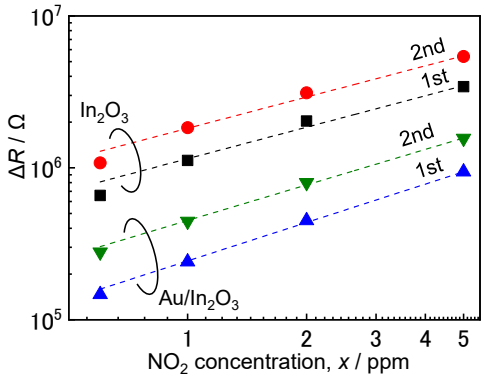

Figure 5. NO_2 concentration dependence of resistance of the In_2O_3 and Au/In_2O_3 sensors in wet air (70%RH at 25 °C) at 100 °C.

Figure 6 shows the response transients to NO_2 (0.1–2 ppm) and the concentration dependences of NO_2 response of the In_2O_3 and Au/In_2O_3 sensors at 100 °C in wet air, together with their *b* values. The baseline resistance did not recover to the initial value either, even if the NO_2 concentration was lower than the case in Figure 3. However, the magnitude of NO_2 responses of both the sensors were also relatively higher than those of the variation in baseline resistance and, thus, the effects of Au loading on the NO_2 sensing properties of these sensors can be discussed. The *b* value of the In_2O_3 sensor was almost the same as that of the Au/In_2O_3 sensor, and both the *b* values were larger than those obtained in the higher NO_2 concentration range at 100 °C (see Table 2). However, the magnitude of the response of the Au/In_2O_3 sensor to NO_2 was higher than that of the In_2O_3 sensor, and the magnitude of the response of the Au/In_2O_3 sensor to 0.1 ppm NO_2 was ca. 133. This is probably due to the smaller resistance of the Au/In_2O_3 sensor in air, which resulted in an increase in the adsorption amount of the negatively charged NO_2 species on the oxide surface. Klein et al. reported that the work function of In_2O_3 was largely dependent on the oxygen concentration during the fabrication process and the subsequent thermal treatment [51]. Sato et al. explained that the work function of In_2O_3 was inversely proportional to $N_e^{2/3}$ (N_e: electron (carrier) density) and the value was estimated to be ca. 5.5 eV in air [52,53]. It is also known that the work function of Au is affected by the measurement conditions, and the value obtained in air was reported 4.60–4.79 eV, which was much smaller than the value observed in the ultrahigh vacuum [54–57]. Therefore, the decrease in base resistance by the loading of Au was probably due to the transfer of the large number of electrons from Au into the conduction band of In_2O_3. These results indicate that the baseline resistance in air is also a key factor for a large amount of the negatively charged NO_2 species. Figure S5 summarizes the relationship between gas adsorption

and depletion layer at both In_2O_3 and Au/In_2O_3 surfaces at 100 °C. In air, a certain number of free electrons of their conduction band is captured by the adsorbed oxygen, which results in the formation of a depletion layer at the surface of the In_2O_3 particles. Since the Au/In_2O_3 has a larger number of free electrons, the thickness of the depletion layer of the Au/In_2O_3 sensor is smaller than that of the In_2O_3 sensor. Under exposure to a low concentration of NO_2, a certain number of negatively charged NO_2 spices is formed on the In_2O_3 and, thus, the thickness of the depletion layer increases. Since the number of free electrons of the Au/In_2O_3 is larger than that of the In_2O_3, the adsorption number of the negatively charged NO_2 species of the Au/In_2O_3 sensor was larger than that of the In_2O_3 sensor. Therefore, the Au/In_2O_3 sensor showed a higher NO_2 response than that of the In_2O_3 sensor, while the adsorption strengths (b) of both the sensors were equally high. When the concentration of NO_2 is high, the b value of the In_2O_3 sensor is lower than that of the Au/In_2O_3 sensor at 100 °C (see Table 2). This fact also affected the adsorption amount of the negatively charged NO_2 species of the Au/In_2O_3 sensor more so than that of the In_2O_3 sensor, leading to a higher NO_2 response.

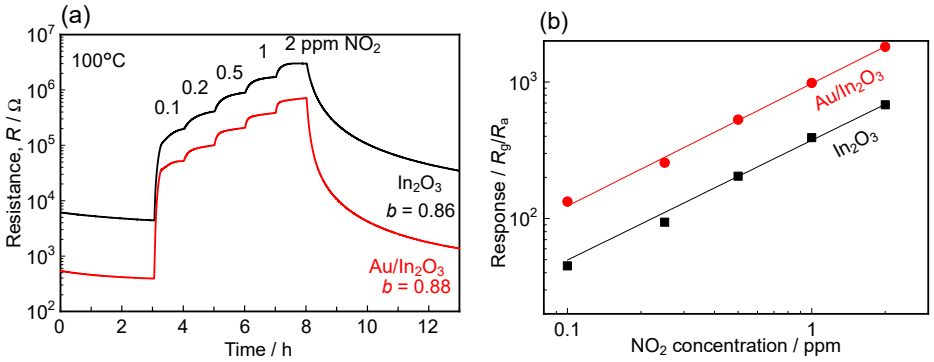

Figure 6. (**a**) Response transients to NO_2 (0.1–2 ppm) and (**b**) concentration dependences of NO_2 response of the In_2O_3 and Au/In_2O_3 sensors at 100 °C in wet air (70%RH at 25 °C).

Figure 7 shows a comparison of the normalized responses of the In_2O_3 and Au/In_2O_3 sensors to 5 ppm NO_2, 200 ppm CO, and 20 ppm C_2H_5OH at 100–300 °C in wet air. The normalized response to CO and C_2H_5OH of the In_2O_3 sensor was very small in the examined operating temperature, while the C_2H_5OH responses of the Au/In_2O_3 sensor were the highest at 200 °C. In addition, the normalized responses to NO_2 of these sensors at 100 °C were higher than those at 200 and 300 °C. Therefore, these sensors showed quite high selectivity to NO_2 at 100 °C when compared with those at 200 and 300 °C. These results confidently concluded that the Au/In_2O_3 sensor showed not only a high response to NO_2, but also excellent NO_2 selectivity against CO and C_2H_5OH.

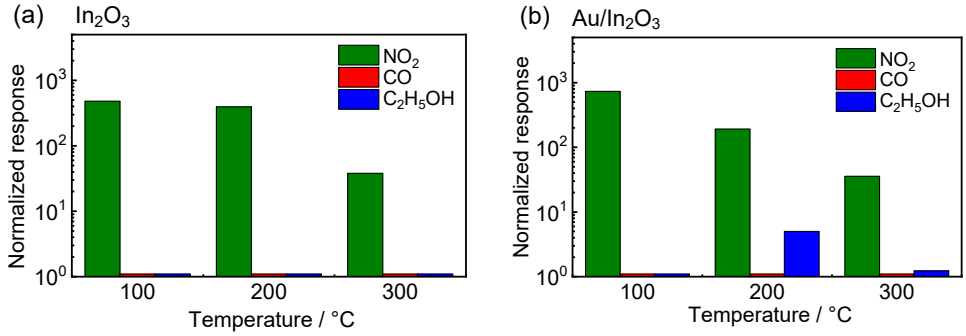

Figure 7. Comparison of normalized responses to 5 ppm NO_2, 200 ppm CO, and 20 ppm C_2H_5OH of the (**a**) In_2O_3 and (**b**) Au/In_2O_3 sensors at 100, 200, and 300 °C in wet air (70%RH at 25 °C).

4. Conclusions

NO_2-sensing properties of the In_2O_3 and Au/In_2O_3 sensors were evaluated in the wet condition, and the effects of the Au loading on the enhancement of NO_2 response were discussed. The baseline resistance in wet air was decreased by the Au loading at all examined temperatures, and the Au/In_2O_3 sensor showed a higher NO_2 response and a faster response speed at lower temperatures (≤100 °C) than those of the In_2O_3 sensor. Notably, the t_{70res} value of the Au/In_2O_3 sensor at 30 °C was much smaller than that of the In_2O_3 sensor, even though the magnitude of response of the Au/In_2O_3 sensor at 30 °C was much higher than that of the In_2O_3 sensor. The adsorption strength (b) of the Au/In_2O_3 sensor at 100 °C was larger than that of the In_2O_3 sensor in the concentration range of 0.6–5 ppm NO_2. The large b value probably induced the larger amount of negatively charged NO_2 species adsorbed on the Au/In_2O_3 surface than that on the In_2O_3 surface, leading to the higher NO_2 response. However, the Au/In_2O_3 sensor also showed much higher NO_2 response than that of the In_2O_3 sensor in the low concentration range of 0.2–2 ppm NO_2, while the b value of the Au/In_2O_3 sensor was almost the same as that of the In_2O_3 sensor. The smaller resistance of the Au/In_2O_3 sensor in air seems to increase the amount of the negatively charged NO_2 species on the oxide surface, especially in the low NO_2 concentration range. In addition, the Au/In_2O_3 sensor showed the excellent NO_2 selectivity against CO and C_2H_5OH.

Supplementary Materials: The following are available online at http://www.mdpi.com/2227-9040/8/3/72/s1, Figure S1: Schematic drawing of (a) sensor element and (b) gas-sensing measurement system., Figure S2: Particle size distribution of precursor mists containing $In_2(NO_3)_3$ and PMMA microspheres prepared by the ultrasonic vibrator, Figure S3: Variations in 70% recovery time (t_{70rec}) of the In_2O_3 and Au/In_2O_3 sensors in wet air (70%RH at 25 °C) with operating temperature, Figure S4: Schematic illustrations of the Gibbs energy diagram for the chemical adsorption of NO_2 over (a) In_2O_3 surface and (b) Au/In_2O_3 surface, Figure S5: Schematic views of gas adsorption properties of In_2O_3 and Au/In_2O_3 surfaces in wet air and NO balanced with wet air at 100 °C.

Author Contributions: Conceptualization, T.U. and N.B.; investigation, T.U. and I.B.; writing—original draft preparation, T.U. and T.H.; writing—review and editing, T.H., Y.S. and N.B.; supervision, U.W. and N.B.; funding acquisition, Y.S. All authors have read and agreed to the published version of the manuscript.

Funding: This study was supported, in part, by the Promotion Program for Strategic International Research Network for accelerating Brain Circulation from the Japan Society for the Promotion of Science (JSPS).

Conflicts of Interest: The authors declare no conflict of interest.

References

1. Taguchi, N. Japanese Patent Application No. 45-38200. 1962.
2. Chiba, A. Development of the TGA gas sensor. In *Chemical Sensor Technology*; Yamauchi, S., Ed.; Kodansha and Elsevier: Amsterdam, The Netherlands, 1992; Volume 4, pp. 1–18.
3. Yamazoe, N. Toward innovations of gas sensor technology. *Sens. Actuators B* **2005**, *108*, 2–14. [CrossRef]
4. Kim, T.-H.; Jeong, S.-Y.; Moon, Y.K.; Lee, J.-H. Dual-mode gas sensor for ultrasensitive and highly selective detection of xylene and toluene using Nb-doped NiO hollow spheres. *Sens. Actuators B* **2019**, *301*, 127140. [CrossRef]
5. Prajapati, C.S.; Bhat, N. Ppb level detection of NO_2 using a WO_3 thin film based sensor: Material optimization, device fabrication and packaging. *RSC Adv.* **2018**, *8*, 6590–6599. [CrossRef]
6. Weinberger, B.; Laskin, D.L.; Heck, D.E.; Laskin, J.D. The toxicology of inhaled nitric oxide. *Toxicol. Sci.* **2001**, *59*, 5–16. [CrossRef]
7. Bernstein, J.A.; Alexis, N.; Barnes, C.; Bernstein, I.L.; Bernstein, J.; Nel, A.; Peden, D.; Sanchez, D.D.; Tarlo, S.M.; Williams, P.B. Health effects of air pollution. *J. Allergy Clin. Immunol.* **2004**, *114*, 1116–1123. [CrossRef] [PubMed]
8. National Ambient Air Quality Standards for Pollutants Considered Harmful to Public Health and the Environment. Available online: https://www.epa.gov/criteria-air-pollutants/naaqs-table (accessed on 10 June 2020).
9. Wang, J.; Zhang, W.; Cao, R.; You, X.; Lai, H. Analysis of nitrogen dioxide in environment. *Adv. Biosci. Biotechnol.* **2016**, *7*, 278–288. [CrossRef]

10. Reference Method for the Determination of Nitrogen Dioxide in the Atmosphere (Chemiluminescence). Available online: https://www3.epa.gov/ttn/amtic/files/ambient/pm25/qa/no2.pdf (accessed on 8 July 2020).
11. Choi, S.-B.; Lee, W.S.; Lee, C.; Lee, S. Enhanced NO_2 gas-sensing performance of Pd/ZnO-codecorated SnO_2 nanorod sensors. *Appl. Phys. A* **2018**, *124*, 817. [CrossRef]
12. Kim, H.J.; Jo, S.B.; Ahn, J.H.; Hwang, B.W.; Chae, H.J.; Kim, S.Y.; Huh, J.S.; Ragupathy, D.; Lee, S.C.; Kim, J.C. SnO_2 nanowire gas sensors for detection of ppb level NOx gas. *Adsorption* **2019**, *25*, 1259–1269. [CrossRef]
13. Wang, Y.; Liu, C.; Wang, Z.; Song, Z.; Zhou, X.; Han, N.; Chen, Y. Sputtered SnO_2: NiO thin films on self-assembled Au nanoparticle arrays for MEMS compatible NO_2 gas sensors. *Sens. Actuators B* **2019**, *278*, 28–38. [CrossRef]
14. Yang, L.; Marikutsa, A.; Rumyantseva, M.; Konstantinova, E.; Khmelevsky, N.; Gaskov, A. Quasi similar routes of NO_2 and NO sensing by nanocrystalline WO_3: Evidence by in situ DRIFT spectroscopy. *Sensors* **2019**, *19*, 3405. [CrossRef]
15. Yan, D.; Li, S.; Liu, S.; Tan, M.; Cao, M. Electrodeposited tungsten oxide films onto porous silicon for NO_2 detection at room temperature. *J. Alloys Compd.* **2018**, *735*, 718–727. [CrossRef]
16. Tamaki, J.; Naruo, C.; Yamamoto, Y.; Matsuoka, M. Sensing properties to dilute chlorine gas of indium oxide based thin film sensors prepared by electron beam evaporation. *Sens. Actuators B* **2002**, *83*, 190–194. [CrossRef]
17. Xu, X.; Zhao, P.; Wang, D.; Sun, P.; You, L.; Sun, Y.; Liang, X.; Liu, F.; Chen, H.; Lu, G. Preparation and gas sensing properties of hierarchical flower-like In_2O_3 microspheres. *Sens. Actuators B* **2013**, *176*, 405–412. [CrossRef]
18. Gao, L.; Cheng, Z.; Xiang, Q.; Zhang, Y.; Xu, J. Porous corundum-type In_2O_3 nanosheets: Synthesis and NO_2 sensing properties. *Sens. Actuators B* **2015**, *208*, 436–443. [CrossRef]
19. Xu, P.; Cheng, Z.; Pan, Q.; Xu, J.; Xiang, Q.; Yu, W.; Chu, Y. High aspect ratio In_2O_3 nanowires: Synthesis, mechanism and NO_2 gas-sensing properties. *Sens. Actuators B* **2008**, *130*, 802–808. [CrossRef]
20. Li, S.; Cheng, M.; Liu, G.; Zhao, L.; Zhang, B.; Gao, Y.; Lu, H.; Wang, H.; Zhao, J.; Liu, F.; et al. High-response and low-temperature nitrogen dioxide gas sensor based on gold-loaded mesoporous indium trioxide. *J. Colloid Interface Sci.* **2018**, *5224*, 368–378. [CrossRef]
21. Steffes, H.; Imawan, C.; Solzbacher, F.; Obermeier, E. Enhancement of NO_2 sensing properties of In_2O_3-based thin films using an Au or Ti surface modification. *Sens. Actuators B* **2001**, *78*, 106–112. [CrossRef]
22. Yu, Y.-T.; Majhi, S.M.; Song, H.-G. Synthesis and gas sensing properties of Au@In_2O_3 core-shell Nanoparticles. *Procedia Eng.* **2016**, *168*, 227–230. [CrossRef]
23. Liu, Y.; Gao, X.; Li, F.; Lu, G.; Zhang, T.; Barsan, N. Pt-In_2O_3 mesoporous nanofibers with enhanced gas sensing performance towards ppb-level NO_2 at room temperature. *Sens. Actuators B* **2018**, *260*, 927–936. [CrossRef]
24. Wang, Z.; Men, G.; Zhang, R.; Gu, F.; Han, D. Pd loading induced excellent NO_2 gas sensing of 3DOM In_2O_3 at room temperature. *Sens. Actuators B* **2018**, *263*, 218–228. [CrossRef]
25. Chen, K.; Lu, H.; Li, G.; Zhang, J.; Tian, Y.; Gao, Y.; Guo, Q.; Lu, H.; Gao, J. Surface functionalization of porous In_2O_3 nanofibers with Zn nanoparticles for enhanced low-temperature NO_2 sensing properties. *Sens. Actuators B* **2020**, *308*, 127716. [CrossRef]
26. Yang, Q.; Wang, Y.; Liu, J.; Liu, J.; Gao, Y.; Sun, P.; Jie, Z.; Zhang, T.; Wang, Y.; Lu, G. Enhanced sensing response towards NO_2 based on ordered mesoporous Zr-doped In_2O_3 with low operating temperature. *Sens. Actuators B* **2017**, *241*, 806–813. [CrossRef]
27. Kim, J.-H.; Mirzaei, A.; Kim, H.W.; Kim, S.S. Low-voltage-driven sensors based on ZnO nanowires for room-temperature detection of NO_2 and CO gases. *ACS Appl. Mater. Interfaces* **2019**, *11*, 24172–24183. [CrossRef] [PubMed]
28. Chena, R.; Wangb, J.; Xiang, L. Facile synthesis of mesoporous ZnO sheets assembled by small nanoparticles for enhanced NO_2 sensing performance at room temperature. *Sens. Actuators B* **2018**, *270*, 207–215. [CrossRef]
29. Dilonardo, E.; Penza, M.; Alvisi, M.; Franco, C.D.; Palmisano, F.; Torsi, L.; Cioffi, N. Evaluation of gas-sensing properties of ZnO nanostructures electrochemically doped with Au nanophase. *Beilstein. J. Nanotechnol.* **2016**, *7*, 22–31. [CrossRef]
30. Degler, D.; Weimar, U.; Barsan, N. Current understanding of the fundamental mechanisms of doped and loaded semiconducting metal-oxide-based gas sensing materials. *ACS Sens.* **2019**, *4*, 2228–2249. [CrossRef]

31. Gurlo, A.; Bârsan, N.; Ivanovskaya, M.; Weimar, U.; Göpel, W. In_2O_3 and MoO_3–In_2O_3 thin film semiconductor sensors: Interaction with NO_2 and O_3. *Sens. Actuators B* **1998**, *47*, 92–99. [CrossRef]
32. Ivanovskaya, M.; Gurlo, A.; Bogdanov, P. Mechanism of O_3 and NO_2 detection and selectivity of In_2O_3 sensors. *Sens. Actuators B* **2001**, *77*, 264–267. [CrossRef]
33. Staerz, A.; Boehme, I.; Degler, D.; Bahri, M.; Doronkin, D.E.; Zimina, A.; Brinkmann, H.; Herrmann, S.; Junker, B.; Ersen, O.; et al. Rhodium oxide surface-loaded gas sensors. *Nanomaterials* **2018**, *8*, 892. [CrossRef]
34. Hashimoto, M.; Inoue, H.; Hyodo, T.; Shimizu, Y.; Egashira, M. Preparation and gas sensor application of ceramic particles with submicron-size spherical macropores. *Sens. Lett.* **2008**, *6*, 887–890. [CrossRef]
35. Hyodo, T.; Inoue, H.; Motomura, H.; Matsuo, K.; Hashishin, T.; Tamaki, J.; Shimizu, Y.; Egashira, M. NO_2 sensing properties of macroporous In_2O_3-based powders fabricated by utilizing ultrasonic spray pyrolysis employing polymethylmethacrylate microspheres as a template. *Sens. Actuators B* **2010**, *151*, 265–273. [CrossRef]
36. Hyodo, T.; Furuno, S.-I.; Fujii, E.; Matsuo, K.; Motokucho, S.; Kojio, K.; Shimizu, Y. Porous In_2O_3 powders prepared by ultrasonic-spray pyrolysis as a NO_2-sensing material: Utilization of polymethylmethacrylate microspheres synthesized by ultrasonic-assisted emulsion polymerization as a template. *Sens. Actuators B* **2013**, *187*, 495–502. [CrossRef]
37. Hyodo, T.; Fujii, E.; Ishida, K.; Ueda, T.; Shimizu, Y. Microstructural control of porous In_2O_3 powders prepared by ultrasonic-spray pyrolysis employing self-synthesized polymethylmethacrylate microspheres as a template and their NO_2-sensing properties. *Sens. Actuators B* **2017**, *244*, 992–1003. [CrossRef]
38. Ueda, T.; Ishida, K.; Kamada, K.; Hyodo, T.; Shimizu, Y. Improvement in NO_2 sensing properties of semiconductor-type gas sensors by introducing a metal into porous In_2O_3 powders. *Front. Mater.* **2019**, *6*, 81. [CrossRef]
39. Yamazoe, N.; Sakai, G.; Shimanoe, K. Oxide semiconductor gas sensors. *Catal. Surv. Asia* **2003**, *7*, 63–75. [CrossRef]
40. Choi, S.-W.; Jung, S.-H.; Kim, S.S. Significant enhancement of the NO_2 sensing capability in networked SnO_2 nanowires by Au nanoparticles synthesized via g-ray radiolysis. *J. Hazard. Mater.* **2011**, *193*, 243–248. [CrossRef]
41. Mun, Y.; Park, S.; An, S.; Lee, C.; Kim, H.W. NO_2 gas sensing properties of Au-functionalized porous ZnO nanosheets enhanced by UV irradiation. *Ceram. Int.* **2013**, *39*, 8615–8622. [CrossRef]
42. Shim, Y.-S.; Moon, H.G.; Kim, D.H.; Zhang, L.; Yoon, S.-J.; Yoon, Y.S.; Kang, C.-Y.; Jang, H.W. Au-decorated WO_3 cross-linked nanodomes for ultrahigh sensitive and selective sensing of NO_2 and C_2H_5OH. *RSC Adv.* **2013**, *3*, 10452–10459. [CrossRef]
43. Miura, N.; Wang, J.; Elumalai, P.; Ueda, T.; Terada, D.; Hasei, M. Improving NO_2 sensitivity by adding WO_3 during processing of NiO sensing-electrode of mixed-potential-type zirconia-based sensor. *J. Electrochem. Soc.* **2007**, *154*, J246–J252. [CrossRef]
44. Kim, C.H.; Qi, G.; Dahlberg, K.; Li, W. Strontium-doped perovskites rival platinum catalysts for treating NOx in simulated diesel exhaust. *Science* **2020**, *327*, 1624–1627. [CrossRef]
45. Roso, S.; Bittencourt, C.; Umek, P.; Gonzalez, O.; Guell, F.; Urakawa, A.; Llobet, E. Synthesis of single crystalline In_2O_3 octahedra for the selective detection of NO_2 and H_2 at trace levels. *J. Mater. Chem. C* **2016**, *4*, 9418–9427. [CrossRef]
46. Srivastava, R.K.; Lal, P.; Dwivedi, R.; Srivastava, S.K. Sensing mechanism in tin oxide-based thick-film gas sensors. *Sens. Actuators B* **1994**, *21*, 213–218. [CrossRef]
47. Fua, H.; Li, Y.; Yua, Z.; Shena, J.; Lia, J.; Zhanga, M.; Dinga, T.; Xua, L.; Lee, S.S. Ammonium removal using a calcined natural zeolite modified with sodium. *J. Hazard. Mater.* **2020**, *393*, 122481. [CrossRef] [PubMed]
48. Dada, A.O.; Olalekan, A.P.; Olatunya, A.M.; Dada, O. Langmuir, Freundlich, Temkin and Dubinin–Radushkevich isotherms studies of equilibrium sorption of Zn^{2+} unto phosphoric acid modified rice husk. *J. Appl. Chem.* **2012**, *3*, 38–45.
49. Roso, S.; Degler, D.; Llobet, E.; Barsan, N.; Urakawa, A. Temperature-dependent NO_2 sensing mechanisms over indium oxide. *ACS Sens.* **2017**, *2*, 1272–1277. [CrossRef]
50. Barsan, N.; Weimar, U. Conduction model of metal oxide gas sensors. *J. Electroceram.* **2001**, *7*, 143–167. [CrossRef]

51. Klein, A.; Körber, C.; Wachau, A.; Säuberlich, F.; Gassenbauer, Y.; Schafranek, R.; Harvey, S.P.; Mason, T.O. Surface potentials of magnetron sputtered transparent conducting oxides. *Thin Solid Films* **2009**, *518*, 1197–1203. [CrossRef]
52. Sato, Y.; Ashida, T.; Oka, N.; Shigesato, Y. Carrier density dependence of optical band gap and work function in Sn-doped In_2O_3 films. *Appl. Phys. Express* **2010**, *3*, 061101. [CrossRef]
53. Sato, Y.; Tokumaru, R.; Nishimura, E.; Song, P.-K.; Shigesato, Y.; Utsumi, K.; Iigusa, H. Structural, electrical, and optical properties of transparent conductive In_2O_3-SnO_2 films. *J. Vac. Sci. Technol. A* **2005**, *23*, 1167–1172. [CrossRef]
54. Tani, T. Analysis of work functions of noble metals in ambient atmosphere in commemoration of journal award. *J. Soc. Photogr. Sci. Technol. Jpn.* **2015**, *78*, 16–22.
55. Manaka, T.; Lim, E.; Tamura, R.; Iwamoto, M. Control of the nano electrostatic phenomena at a pentacene/metal interface for improvement of the organic FET devices. *Thin Solid Films* **2006**, *499*, 386–391. [CrossRef]
56. Yamashita, D.; Ishizaki, A. In situ measurements of change in work function of Pt, Pd and Ausurfaces during desorption of oxygen by using photoemission yield spectrometer in air. *Appl. Surf. Sci.* **2016**, *363*, 240–244. [CrossRef]
57. Wan, A.; Hwang, J.; Amy, F.; Kahn, A. Impact of electrode contamination on the a-NPD/Au hole injection barrier. *Org. Electron.* **2005**, *6*, 47–54. [CrossRef]